Optical and structural properties of *p*-doped Ge/SiGe multiple quantum wells for mid-infrared photonics

Stefano Calcaterra,[1] Marco Faverzani,[1] Davide Impelluso,[1] Daniel Chrastina,[1] Raffaele Giani,[1] Luca Anzi,[1] Jin H. Bae,[2] Camillo Tassi,[3] Dan Buca,[2] Paolo Biagioni,[1] Giovanni Isella,[1] Michele Virgilio,[3] and Jacopo Frigerio[1,*]

[1]*Dipartimento di Fisica, Politecnico di Milano, Piazza L. da Vinci, 32, 20133 Milano, Italy*
[2]*Peter Grünberg Institute 9 (PGI 9), Forschungszentrum Jülich, 52428 Jülich, Germany*
[3]*Dipartimento di Fisica "E. Fermi", Università di Pisa, Largo Pontecorvo, 3, 56127 Pisa, Italy*

(Received 3 March 2025; revised 28 May 2025; accepted 23 June 2025; published 28 July 2025)

We present a detailed study of hole-doped Ge/SiGe multiple quantum wells as a promising material platform for mid-infrared photonics. The heterostructures were grown on SiGe virtual substrates using low-energy plasma-enhanced chemical vapor deposition. Structural and compositional analyses via atom probe tomography and x-ray diffraction were employed to assess the crystal quality and retrieve the compositional profiles. The optical response of the samples, in the 4–12-μm wavelength range, was investigated as a function of the temperature and complementary Hall-effect measurements were performed providing insights into the temperature evolution of the electrical transport properties. In addition, a well-established tight-binding model was used to reproduce and interpret the experimental results starting from the calculated valence band structure.

DOI: 10.1103/9mm6-96nk

I. INTRODUCTION

The mid-infrared (MIR) is a spectral range hosting the so-called "fingerprint" region (wavelengths from 6 to 15 μm) where most molecules feature vibrational resonances. In the last decade, remarkable research efforts have been made to develop integrated photonic devices operating in the MIR spectral region to detect, identify, and potentially quantify chemical and biological substances. The fields of application are several and include detection of traces of greenhouse and toxic gases [1], monitoring of industrial emissions [2], and detection of molecules for medical diagnostics [3] as well as astronomical observations [4].

Different material platforms are under consideration to develop MIR photonic integrated circuits, including III-V semiconductors [5], chalcogenide glasses [6], and group-IV semiconductors. Among these, Si-based materials are deemed very promising since they provide compact, high-density photonic platforms and can benefit from cutting-edge fabrication tools and large wafer sizes commonly used in the microelectronic industry. Standard silicon-on-insulator technology is the preferred choice for the short-range MIR ($\lambda < 4\,\mu$m) [7], but the strong absorption that occurs in the SiO_2 cladding layers prevents addressing longer wavelengths [8]. This challenge has been overcome using Ge-on-Si and SiGe-on-Si material platforms, where it is possible to take advantage of the high MIR transparency of Ge to cover the full 3–15-μm spectral range. Several photonics building blocks have been already demonstrated on both platforms [9], nevertheless key functionalities such as photodetection and high-speed modulation have seldom been investigated [10,11]. A possible approach to tackle such challenges is to exploit intersubband transitions (ISBTs) in hole-doped Ge/SiGe quantum wells (QWs). The choice of a hole-based heterostructure is motivated by the larger offsets, up to 300 meV, occurring in the valence band of Ge/SiGe QWs, as required to design ISBTs falling in the MIR spectral range, while those occurring in the conduction band, and specifically in the *L* valley, are limited to 100–150 meV, making them suitable for far-infrared applications [12–14]. Up to now, ISBTs in hole-doped SiGe heterostructures have been mainly investigated in Si/SiGe QWs [15–18] grown on Si-rich SiGe virtual substrates (VSs). This choice has been motivated by the significantly easier epitaxial procedure required for obtaining Si-rich relaxed SiGe VSs.

The interest in Ge/SiGe QWs [19–21] deposited on Ge-rich SiGe VSs has increased only recently, due to the compatibility with the SiGe-on-Si MIR photonic platform and to the advancements of the epitaxial growth techniques, which now allow for the growth of fully relaxed Ge-rich SiGe VSs with a very high crystal quality. Here it should also be mentioned that Ge/SiGe QWs benefit from the lower effective mass of heavy holes in Ge ($0.33m_e$) with respect to that in Si ($0.49m_e$), allowing for ISBTs with a superior oscillator strength with respect to Si/SiGe QWs. This study conducts a detailed investigation into the structural, electrical, and optical properties of *p*-doped Ge/SiGe multiple quantum wells (MQWs) with the goal of establishing a robust theoretical and experimental foundation to evaluate the potential and limitations of this material platform for developing advanced MIR

*Contact author: jacopo.frigerio@polimi.it

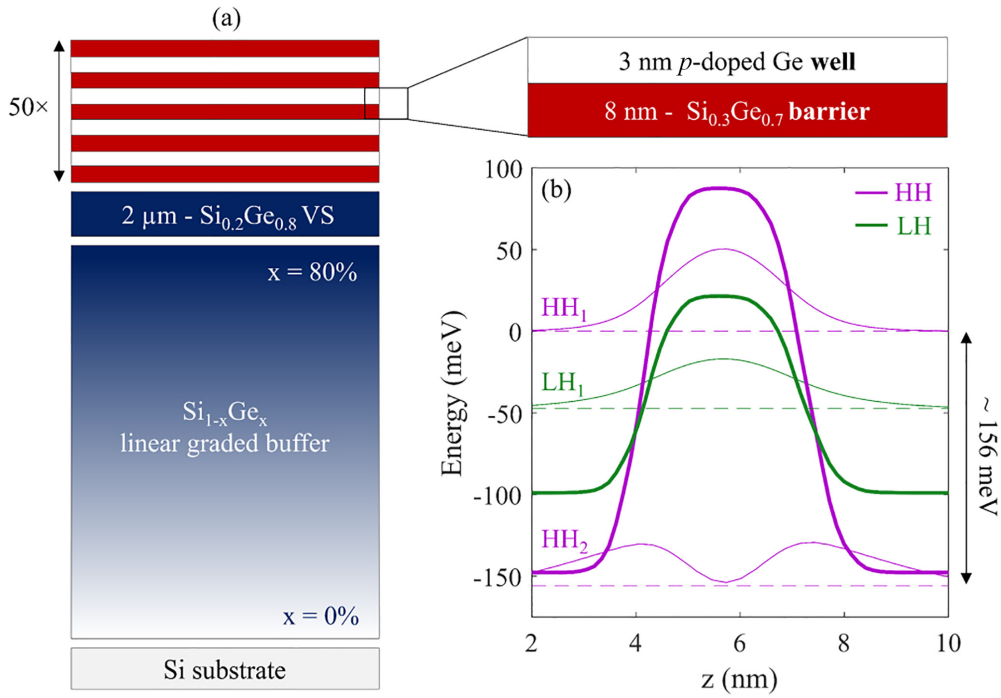

FIG. 1. Basic structure of the investigated samples. (a) Schematic of the sample showing detailed epitaxial steps. (b) Band-edge profiles, confined energy levels, and corresponding wave functions.

photonic devices, including intersubband quantum-confined Stark effect modulators and QW infrared photodetectors (QWIPs).

II. DESIGN AND EPITAXIAL GROWTH OF THE QUANTUM WELLS

The heterostructure investigated in this paper features hole-doped 3-nm-thick Ge QWs sandwiched between 8-nm-thick $Si_{0.3}Ge_{0.7}$ barriers coherently grown on a $Si_{0.2}Ge_{0.8}$ VS, as schematically shown in Fig. 1(a). The Si content difference in the MQW layers compared to the VS leads to built-in biaxially compressive strain in the Ge wells and biaxially tensile strain in the $Si_{0.3}Ge_{0.7}$ barriers, whose thickness has been chosen to balance the strain in each barrier-QW period. Furthermore, a 1-nm-wide intermixing region between the wells and the barriers has been included in the nominal design, building on previous works done with similar heterostructures [18]. Based on this profile, the electronic structure of the system was analyzed using a first-neighbor $sp^3d^5\sigma^*$ tight-binding Hamiltonian model [22–24] relying on the semiempirical self- and hopping-energy parameters proposed by Boykin *et al.* [25] combined with the associated scaling exponent derived by Jancu *et al.* [26] which allowed for the accurate description of the strong nonparabolicity, band mixing, and spin-orbit interaction occurring in the valence band. The squared moduli of the resulting wave functions, calculated at Γ, are shown in Fig. 1(b). The ground state HH_1 in the Ge well belongs to the heavy hole (HH) band and its energy has been set to 0 eV while the first excited level HH_2 lies at −156 meV. The light hole (LH) subband instead confines a single energy level LH_1 at an energy of around −48 meV. This heterostructure is thus expected to feature a TM-polarized ISBT between the HH_1 and HH_2 hole states at an energy of about 156 meV ($\lambda \simeq 8\,\mu m$). It is noteworthy that the HH_2 state lies just 8 meV above the edge of the potential well, an intentional result of the design aimed at positioning an excited state nearly resonant with the barrier height in order to facilitate the extraction of photoexcited carriers, a desired feature for efficient QWIPs.

The samples have been grown on a 100-mm *p*-Si(001) substrate (resistivity 1–10 Ω cm) by low-energy plasma-enhanced chemical vapor deposition (LEPECVD) [27]. The first part of the stack consists of a forward graded buffer, in which the Ge concentration is varied linearly from 0 to 80% with a constant grading rate of 7%/µm, while the temperature is linearly decreased from 720 to 550 °C to mitigate strain-induced surface roughening. To achieve full relaxation, a 2-µm-thick $Si_{0.2}Ge_{0.8}$ layer has been grown on top of the graded buffer. This serves as a VS for the growth of the MQWs stack as shown in Fig. 1(a). The QWs were *in situ p* doped by adding a spike of B_2H_6, as a precursor gas for boron, in the center of the wells themselves, targeting a doping density of 5×10^{11} cm^{-2} (sample A) and 2.5×10^{12} cm^{-2} (sample B) in each QW. Due to the thinness of the QWs and the high compositional difference between QWs and barriers, interdiffusion can strongly influence the optical properties. The strategy employed to minimize interdiffusion consists of (i) reducing the growth temperature from 550 to 400 °C for the MQWs stack; (ii) interrupting the growth for 30 s before and for 10 s after the growth of the QWs; (iii) reducing the growth rate to around 10 nm/min by controlling the precursor gas (SiH_4, GeH_4) flows. The last step assures a high control of the compositional profile and mitigates the vacancy-assisted interdiffusion, since the vacancy concentration increases with increasing growth rate in the LEPECVD system [28].

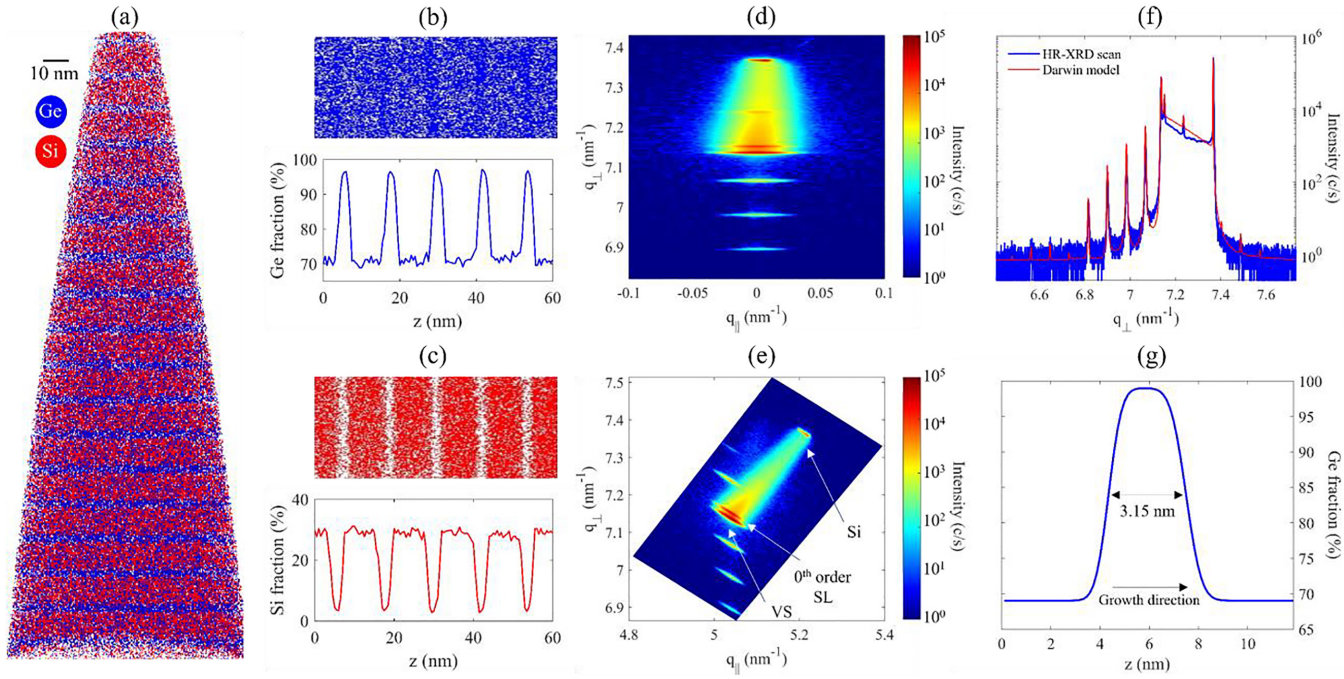

FIG. 2. Structural characterization of the investigated samples. (a) APT data. (b) Ge, and (c) Si content profile across five periods of the MQW structure (d) (004) and (e) (224) RSMs. (f) Experimental ω-2θ scan (blue) and fitting with Darwin model (red). (g) Average compositional profile retrieved from APT and HR-XRD.

III. STRUCTURAL CHARACTERIZATION

The samples have been structurally characterized with two main objectives: to verify the crystal quality of the material and to experimentally determine the actual compositional profile of the MQWs. These data were then used to further refine the band-structure calculations. Due to the small dimensions of the quantum wells, precise structural characterization required advanced techniques such as atom probe tomography (APT) and high-resolution x-ray diffraction (HR-XRD).

The elemental atoms' localization is determined, together with the layer stoichiometry, by APT [Fig. 2(a)]. Reconstructed APT elemental maps along with the composition of a central part with five quantum wells are provided in Figs. 2(b) and 2(c). The SiGe barriers have a Si and Ge concentration of 30% and 70% respectively, which is in agreement with the designed heterostructures. The excellent epitaxial control is demonstrated by the sharpness of the Si profile at the SiGe/Ge interface. The Ge wells, forming the active region of the ISBT device, have an APT determined thickness of 2.84 nm, in full agreement with the XRD data (below).

HR-XRD measurements have been performed with a PANanalytical X'Pert PRO MRD diffractometer. The (004) and (224) reciprocal space maps (RSMs) of sample B are shown in Figs. 2(d) and 2(e) respectively. Regular periodicity of the MQWs' structure is confirmed as well as the lattice-matched growth of the MQWs on the VS, even though the average Ge content in a single superlattice period is approximately 2% lower than in the VS, as indicated by the 0th order peak not being superimposed to the VS peak. The characterization results of both APT and HR-XRD have been employed to retrieve the real compositional profile of the QWs. First of all, the Ge content of each well, as measured by APT, has been extracted and fit independently with the following equation, defined as the sum of two error functions representing the two interfaces of the QW:

$$x(z) = x_l \mathrm{erf}\left(\frac{z - z_l}{\sigma_l}\right) + x_r \mathrm{erfc}\left(\frac{z - z_r}{\sigma_r}\right) + x_{\mathrm{bg}}, \qquad (1)$$

where l and r stand for the left and right interface respectively, and the background term x_{bg} takes into account the fact that the Ge content in the barriers is around 70%. The functional form obtained by APT was then employed to simulate the (004) ω-2θ HR-XRD scan as shown in Fig. 2(f) using the dynamical diffraction Darwin model from xrayutilities [29,30]. The maximum Ge content in the QWs has been adjusted with respect to the value 96.5% extracted by APT to properly fit both the low and the high order diffraction peaks, obtaining 98.9%. The resulting compositional profile is shown in Fig. 2(g). The thickness of each QW, defined as the full width at half maximum (FWHM) of the fitting function is 3.15 ± 0.18 nm, while the period (total QW and barrier thickness) is 11.64 ± 0.52 nm. The profile is slightly asymmetric, with $\sigma_r = 0.7 \pm 0.11$ nm, while $\sigma_l = 0.6 \pm 0.16$ nm. Such asymmetry has been attributed to the differing timing of growth interruptions before and after the Ge well growth.

IV. OPTICAL CHARACTERIZATION

The MIR optical properties of the samples were investigated by means of Fourier-transform infrared (FTIR) spectroscopy employing a commercial spectrometer (Bruker Invenio) equipped with a liquid-nitrogen-cooled mercury cadmium telluride photodetector and a closed-circuit helium cryostat (Oxford OptistatDry BLV). In order to induce ISBT-related absorption a normal incidence geometry cannot be

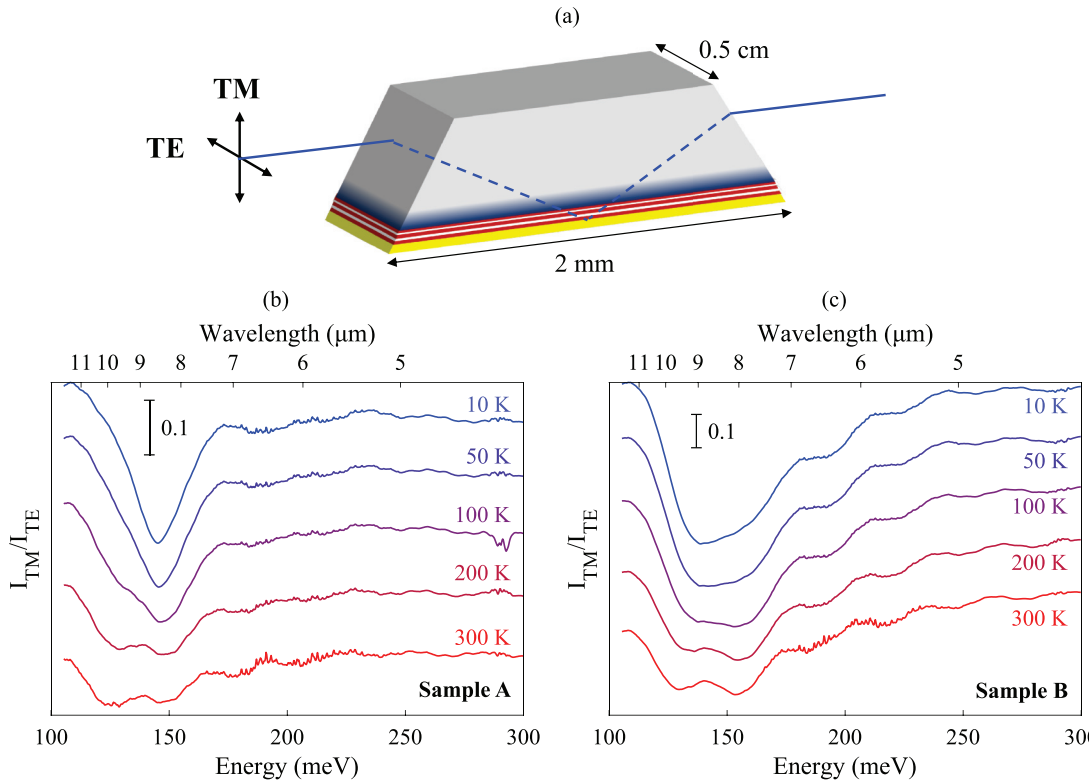

FIG. 3. Optical characterization of the investigated samples. (a) Sketch of the prismlike waveguide geometry showing the Si substrate (grey) the MQW stack (red and white) and the Ti/Au layer (yellow). Temperature-dependent dichroic transmission spectra of (b) sample A and (c) sample B. The sharp features appearing at around 290 meV in the sample A spectrum acquired at 100 K are related to the asymmetric stretching mode of the C-O bonds in CO_2 molecules.

adopted because of the polarization selection rules governing such optical transitions. For this reason, the samples were shaped in the prismlike waveguide geometry shown in Fig. 3(a) with the entrance and exit facets forming angles of 70° with the heterostructure planes so that the light in the MQWs region can be either TM-polarized, i.e., the electric field oscillates along the growth direction, or TE-polarized; i.e., electric field oscillates perpendicular to the growth direction, thus inducing ISBTs or not, depending on the polarization of the impinging light. To enhance the TM component of the electric field in the MQW region a thin metallic layer (Ti/Au, 10/150 nm) was also evaporated on top of the MQWs.

The transmission spectra for both TM and TE polarization were acquired, and the dichroic spectrum was eventually calculated taking the ratio between these two: in doing so, all contributions coming from unpolarized absorption mechanisms were removed highlighting TM- and TE-polarized absorption features which appear as dips and peaks respectively. The dichroic spectra of samples A and B are shown in Figs. 3(b) and 3(c), where temperature-dependent features at energies between 120 and 175 meV can be clearly seen.

The low temperature spectrum of sample A exhibits a clear dip at 145 meV with a FWHM of about 25 meV which can be attributed to the TM-polarized ISBT occurring between the ground and the first excited state of the HH subband. As the temperature increases, a second dip arises at gradually lower energy, eventually reaching the same intensity of the primary peak at room temperature. Sample B clearly shows two broader and partially overlapping dips around 150 meV even at 10 K which increasingly splits with temperature. Moreover, further absorption features appearing at higher energies were observed, together with some Fabry-Perot-like interference fringes which are indeed weakly dependent on temperature and strongly influenced by the prism wave-guide fabrication.

The main mechanisms determining the broadening of the absorption linewidth are the scattering events related to ionized impurities, interface roughness, and alloy scattering [31]. As the structural characterization highlighted, a significant entropic interdiffusion is present which, on one hand, promotes the presence of silicon not only in the barriers but also in the wells, thus introducing alloy scattering, while on the other hand prevents the formation of sharp interfaces, thus reducing the effect of interface roughness. Moreover, on the dimensional scale explored by APT we did not observe any modulation of the QW planes whereas on a longer-range scale, i.e., a few microns, some slight variations are expected, which tentatively contribute to a nonhomogeneous broadening of the linewidth. Both these effects equally contribute to the linewidth broadening of the two samples. On the contrary, ionized impurities scattering is expected to be much stronger in sample B than in sample A because of the doping levels differing by a factor of 5.

The complex evolution of the spectra at different temperatures cannot be explained by merely considering the envelope-function energy levels corresponding to the eigenenergies of the system at the Γ point, because the strong nonparabolicity of the valence band plays a key role in de-

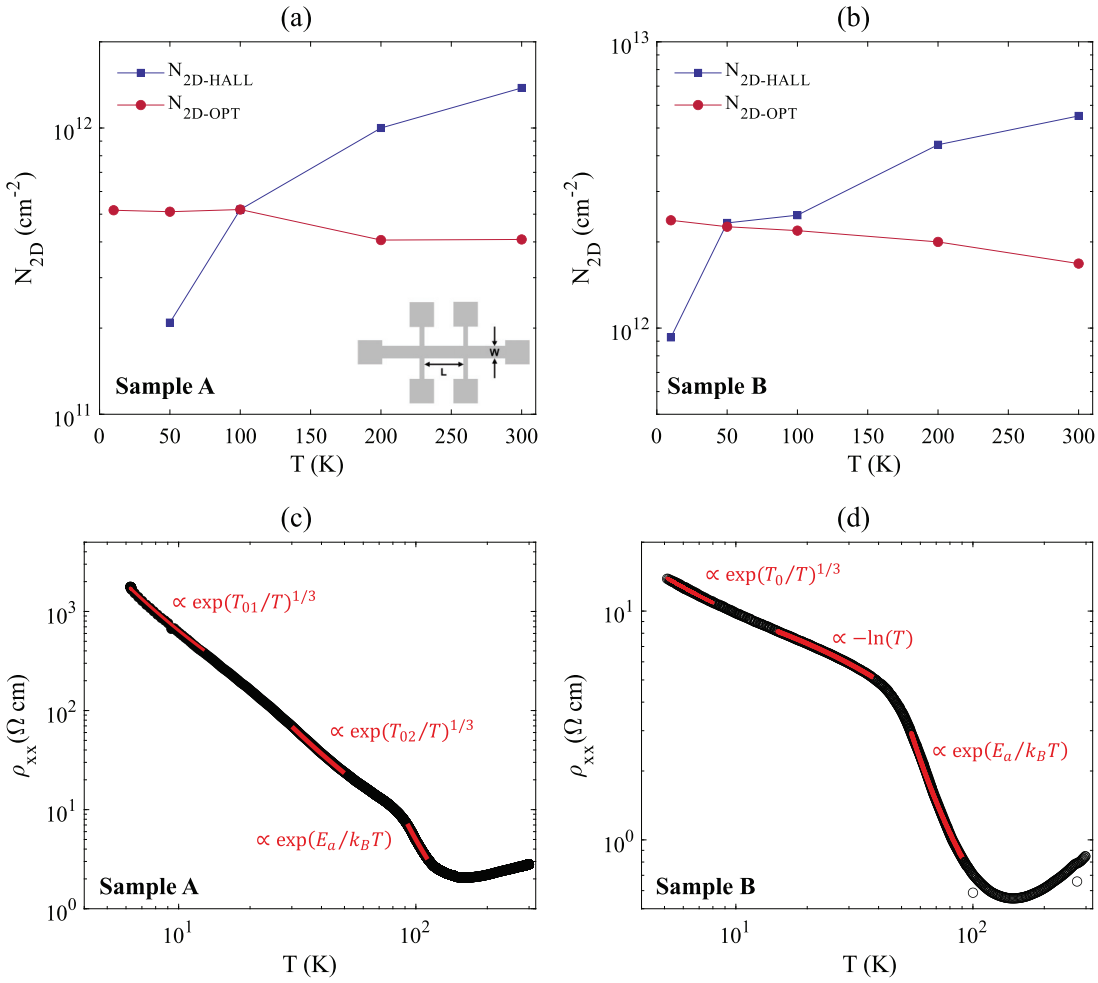

FIG. 4. Hole densities as measured by Hall effect and as retrieved by the dichroic spectra for (a) sample A and (b) sample B. Longitudinal resistivity $\rho_{xx}(T)$ of sample (c) A and (d) sample B.

termining the optical properties of the two samples. For this reason, numerical calculations of the absorption spectra have been performed considering the band structure dispersion in the whole reciprocal space. Running such calculations requires the knowledge of the hole density N_{2D} in the QWs as a function of the temperature which can be extracted from the integral of the experimental absorption spectrum [32] with the formula

$$N_{2D} = \frac{2m^* c\varepsilon_0 n}{\pi e^2 \hbar} \frac{1}{f} \int \alpha_{2D}(E) dE, \tag{2}$$

where m^* is the effective mass and f is the oscillator strength, here set to 1. Despite the nonparabolicity, the HH effective mass at Γ was considered because of the moderate doping levels. The two-dimensional absorption coefficient can be retrieved from the dichroic spectrum as

$$\alpha_{2D} = -\frac{\ln(I_{TM}/I_{TE})}{CMN} \frac{\cos\theta}{\sin^2\theta}, \tag{3}$$

where C is the field enhancement provided by the gold layer, $M = 2$ is twice the number of reflections in the waveguide, $N = 50$ is the number of QWs, and $\theta = 57°$ is the propagation angle with respect to the growth direction in the MQW region. The wavelength-dependent enhancement factor C was evaluated by averaging the $\cos^2(k_z z)$ behavior of the standing wave intensity in the MQW region. The hole densities $N_{2D\text{-}OPT}$ retrieved from the dichroic spectra are reported in Figs. 4(a) and 4(b) for samples A and B respectively, finding values which, at low temperature, nicely agree with the nominal ones.

V. ELECTRICAL CHARACTERIZATION

In order to have also an additional estimation of the hole density, temperature-dependent Hall-effect measurements were run between 10 and 300 K at magnetic fields up to 6 T in a closed-cycle cryostat on Hall bar structures with $W = 100\,\mu m$ and $L = 340\,\mu m$ [see Fig. 4(a)] patterned by photolithography and reactive ion etching. Bonding pads were formed by e-beam evaporation of a Ti(5 nm)/Au(150 nm) metal stack. The hole densities $N_{2D-HALL}$ measured by Hall effect are reported in Figs. 4(a) and 4(b) for samples A and B respectively. It was not possible to measure the hole density at 10 K for sample A because the contacts have a rectifying behavior at this temperature.

Quite surprisingly, the optical and electrical characterizations yielded significantly different results. According to the optical measurements, the hole density in both samples

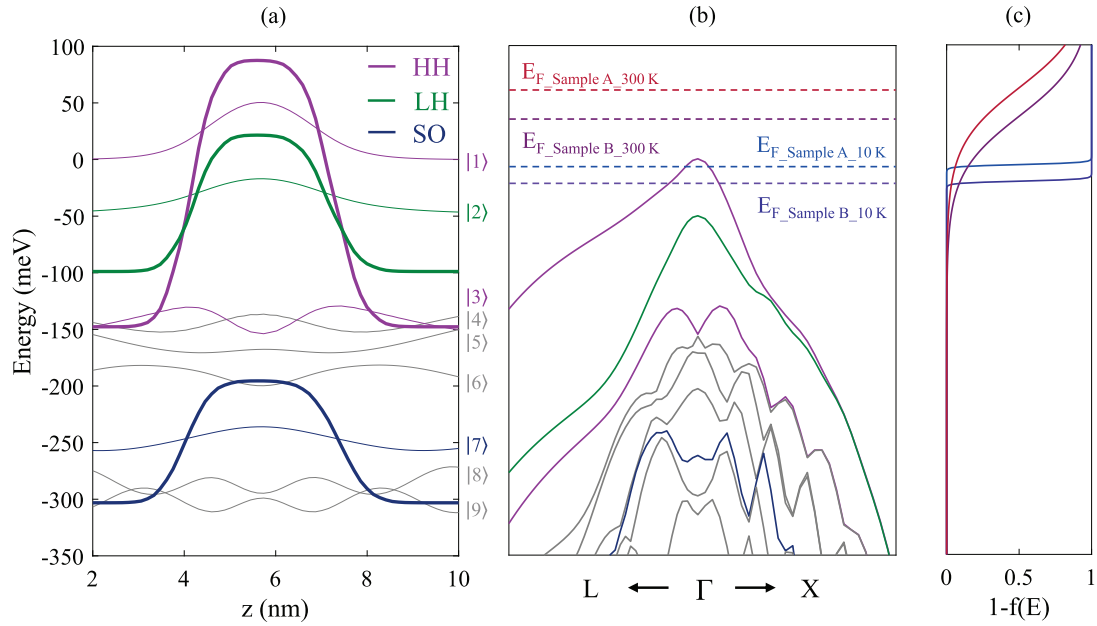

FIG. 5. Electronic band structure and occupation of the energy levels. (a) Valence band energy levels and corresponding wave functions at Γ also including above-band-edge levels. Each energy level has also been identified by a number in progressive order starting from the fundamental level HH_1. (b) Dispersion of the energy bands in the reciprocal space and Fermi levels. (c) Fermi-Dirac occupation function at 10 and 300 K for samples A and B.

reaches the maximum value at 10 K ($5.16 \times 10^{11}\,\mathrm{cm}^{-2}$ for sample A and $2.38 \times 10^{12}\,\mathrm{cm}^{-2}$ for sample B) and then slightly decreases as the temperature increases, reaching respectively $4.08 \times 10^{11}\,\mathrm{cm}^{-2}$ and $1.68 \times 10^{12}\,\mathrm{cm}^{-2}$ at room temperature. The Hall measurements instead show an opposite behavior, where the hole density is minimum at low temperature and then increases as the temperature is increased. Such discrepancy between optical and electrical measurements has been already observed in the literature [33], at least at low temperature, and it was attributed to carrier trapping in localized states making them available for ISBTs but not for band transport.

In order to gain a better understanding of the opposite trends of the hole densities retrieved from the dichroic spectra and measured by Hall effect, the longitudinal resistivity $\rho_{xx}(T)$ as a function of the temperature has been measured for both samples, and the results are reported in Figs. 4(c) and 4(d) for samples A and B respectively. Between 5 and 60 K, the resistivity of sample A follows the relationship $\rho_{xx}(T) \propto \exp[(T_0/T)^{1/3}]$, a signature of variable range hopping (VRH) transport [34]. It was not possible to fit $\rho_{xx}(T)$ with a single characteristic temperature T_0 between 5 and 60 K finding $T_{01} = 12.5$ K and $T_{02} = 21.5$ K below 10 K and between 20 and 60 K, respectively. The characteristic temperature increase suggests that holes can access more distant or higher energy localized states with increasing temperature, thus changing the dominant hopping paths. Above 90 K, the resistivity sharply drops, following the relationship $\rho_{xx}(T) \propto \exp(E_a/kT)$ where $E_a = 35$ meV represents the activation energy, indicating the onset of band transport. The resistivity increases with temperature above 200 K, probably because of phonon scattering. Regarding sample B, at low temperature (up to 10 K), the transport is once again dominated by VRH. Since T_0 is inversely proportional to both the density of states and the localization length, a lower characteristic temperature is expected, as higher dopant concentrations increase both parameters: accordingly, a value of $T_0 = 3.1$ K was obtained. Between 15 and 40 K the resistivity decreases as $\rho_{xx}(T) \propto -\ln T$, indicating that the transport may be controlled by weak localization [35]. Above $T = 50$ K, band transport starts becoming the dominant transport mechanism with an activation energy of 15 meV, smaller than that of sample A. Although accurately modeling impurity states is extremely difficult, the reduction in activation energy with increasing doping is expected as higher doping concentrations leads to the broadening of the impurity levels resulting in the formation of an impurity band due to dopant wave-function overlap [36].

A more in-depth analysis of the transport properties goes beyond the scope of this work, however, the measurements carried out allow us to explain the discrepancy between the Hall and optical measurements. In the VRH regime, only a fraction of the holes present in the system actively participate in conduction, while many of them remain localized due to insufficient thermal energy to enable hopping, thus explaining why $N_{\text{2D-OPT}}$ is higher than $N_{\text{2D-HALL}}$ at low temperature. On the other hand, as the temperature increases, holes start to populate upper bands (e.g., the LH band) following the Fermi-Dirac distribution, but only those lying in the ground state HH_1 are available for ISBTs in the considered energy range, thus clarifying why $N_{\text{2D-OPT}}$ is lower than $N_{\text{2D-HALL}}$ at higher temperature. Hence, $N_{\text{2D-OPT}}$ is the most suitable parameter to be considered for the numerical calculation of the absorption spectra.

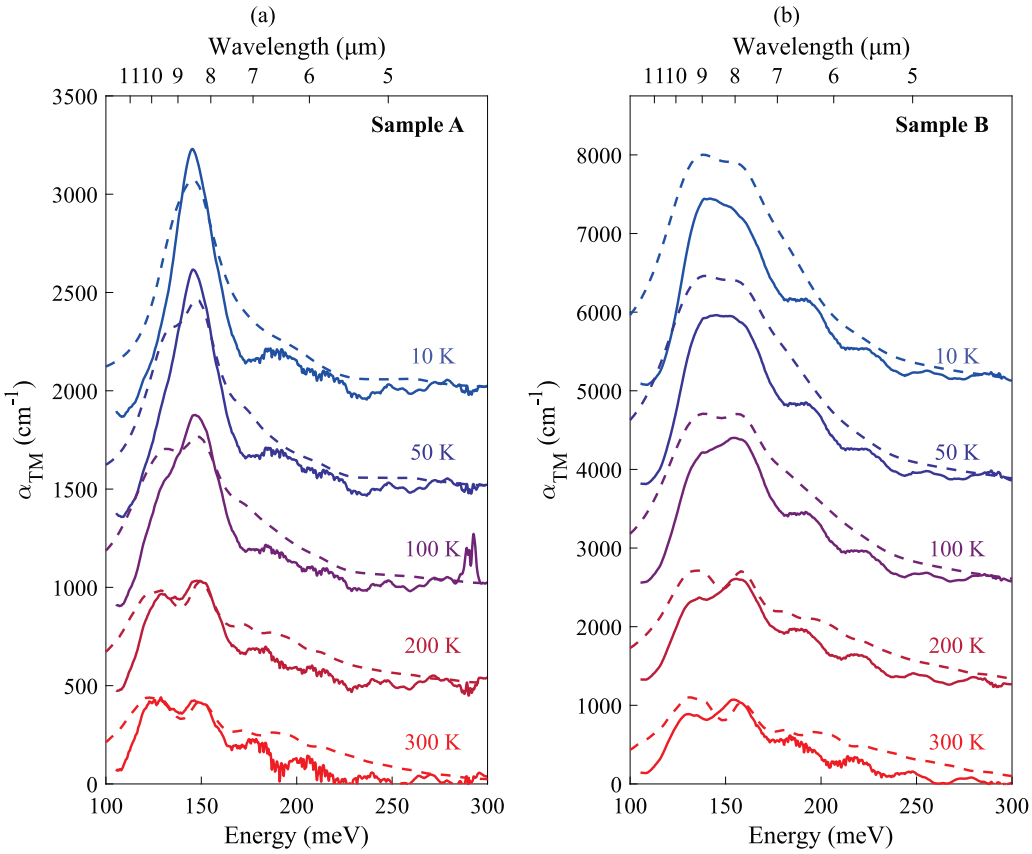

FIG. 6. Temperature-dependent experimental (continuous line) and theoretical (dashed line) absorption coefficients for TM-polarized light of (a) sample A and (b) sample B. The sharp features appearing at around 290 meV in the sample A spectrum acquired at 100 K are related to the antisymmetric stretching mode of the C-O bonds in CO_2 molecules.

VI. DISCUSSION

Having characterized the samples from the structural, optical, and electrical points of view, it is now possible to numerically compute the absorption spectra and understand the evolution of their optical properties with the temperature. As a first step, the band structure in the whole reciprocal space has been calculated. Since no substantial modifications are expected for the considered doping levels, the hole density was only taken into account to determine the occupancy of each state; similarly, temperature-dependent modifications of the electronic spectrum have been neglected. The energy levels at Γ as well as the corresponding eigenstates are shown in Fig. 5(a) while Fig. 5(b) reports the band structure dispersion along the Γ-to-*L* and Γ-to-*X* directions. It is worth noticing that, besides the HH_2 level, two further states which are almost degenerate with the top of the barrier are present.

The absorption coefficient can be theoretically computed starting from the band structure applying Fermi's "golden rule." A phenomenological broadening was considered using a Lorentzian line shape with the same width for all active ISBTs. At 10 K, the FWHM was set to approximately 20 and 32 meV for samples A and B, respectively. At higher temperatures, the broadening parameter was slightly adjusted by fitting the measured single peak feature. The hole density evolution with the temperature must also be explicitly included in the calculation of the optical spectra through Fermi-Dirac statistics since it determines the occupation of the energy levels. At all temperatures, the experimentally determined $N_{2D\text{-}OPT}$ values were used. Figure 5(c) shows the Fermi- Dirac distribution functions at low and high temperature for both samples. The experimental *effective* absorption coefficients, calculated from α_{2D} dividing by the period of the heterostructure, and the theoretical absorption spectra of samples A and B are reported in Figs. 6(a) and 6(b). In both cases, the calculated spectra well reproduce the main experimental features both qualitatively and quantitatively, despite that the adopted model does not account for any many-body effects related to electron-electron interaction, which include exchange correlation, depolarization shift, and excitonic shift [32]. The depolarization shift can be estimated based on the hole sheet density and the electronic wave functions [15,37], typically resulting in a blueshift of a few meV. To align the calculated spectra with the experimental peak positions, blueshifts of 3 and 12 meV were applied in Figs. 6(a) and 6(b), respectively. These values are consistent with the estimated depolarization shift, which is expected to be more pronounced in sample B due to its higher doping density.

The low-temperature spectrum of sample A only shows a Lorentzian peak which can be naively assigned to ISBTs occurring between the HH_1 and HH_2 energy levels. When increasing the temperature, secondary spectral features arise, as

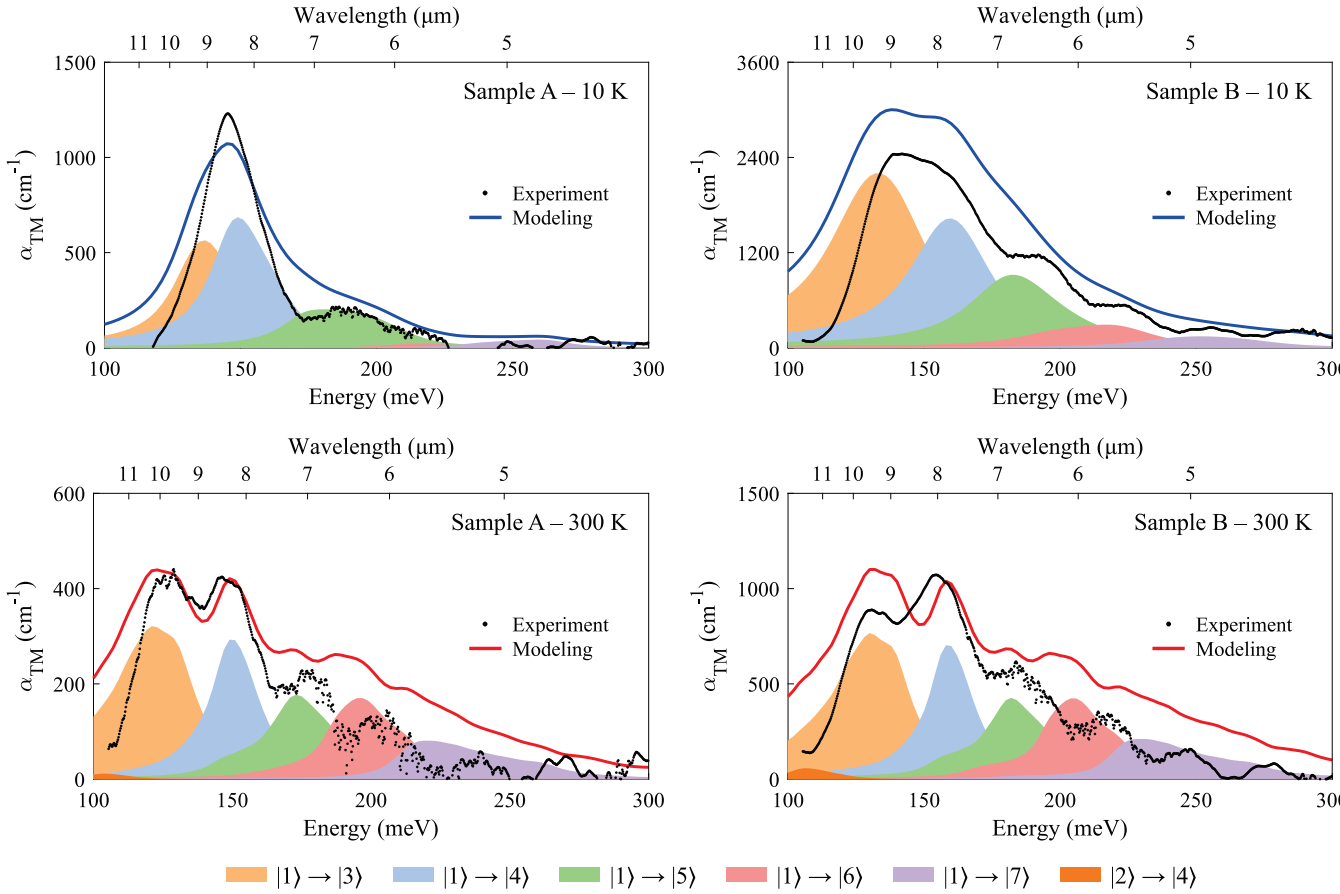

FIG. 7. Theoretical and experimental absorption coefficients of both samples at 10 and 300 K. The individual contributions to the theoretical absorption spectra coming from different ISBTs are separated into distinct peaks labeled according to the level numbering introduced in Fig. 5(a).

also predicted by the numerical calculations. Similar considerations apply also to sample B for which, however, other ISBTs are already active even at 10 K. To gain further insight into the optical transitions which contribute to the observed features, the theoretical spectra were deconvolved discerning among ISBTs involving different initial and final states, labeled as in Fig. 5(a). Figure 7 shows the comparison between the experimental effective absorption coefficients and the corresponding theoretical curves of both samples at 10 and 300 K where the various contributions are highlighted. The spectra shown in Fig. 5(a) indicate that the *splitting* of the main peak, either observed by increasing the Fermi energy or the temperature, which in turn modifies the chemical potential [38], is related to the activation of ISBTs which involve both the $|3\rangle$ and $|4\rangle$ levels, in a region of the reciprocal space where these two subband states have a larger energy separation. Indeed, $|3\rangle$ and $|4\rangle$ result from the interaction of HH_2 and LH_2, and the presence of a nonvanishing $k_{\|}$ momentum induces a redistribution of the TM oscillator strength in favor of the latter state making both these transitions observable. Furthermore, the negative curvature of the HH_2 state, which can be ascribed to the valence-band nonparabolicity, introduces a significative reshaping of the single absorption peaks. It is also worth noting that, at room temperature, ISBTs starting from the LH_1 level, labeled as $|2\rangle$ in Fig. 5(a), contribute to the absorption spectra of both samples, as the exponential tail of the Fermi-Dirac distribution functions of Fig. 5(c) manages to reach LH_1 level, thus suggesting that a non-negligible fraction of the carriers occupies this state.

VII. CONCLUSIONS AND PERSPECTIVES

In this work, we investigated ISBTs in the MIR spectral range in hole-doped Ge/SiGe QWs, featuring nanometer-sized epilayers and significant well/barrier alloy contrasts. Strong TM-polarized ISBT absorption features were observed, with peak absorption coefficients exceeding 1000 cm^{-1} at room temperature. By combining a thorough structural characterization with advanced theoretical modeling, we accurately captured the evolution of the optical absorption spectra as a function of both temperature and doping density, achieving excellent agreement with experimental results.

Our findings establish a robust theoretical and experimental foundation for understanding the structural and optical properties of hole-doped Ge/SiGe QWs, paving the way for their integration into MIR photonic integrated devices.

ACKNOWLEDGMENTS

This research has received funding from the European Union, Next Generation EU, “Fondo PRIN 2022”, germanium Quantum wells for SENSing in the mid-infrarEd, id:

2022X5CXTJ, Grant No. CUP: D53D23002450001. This research has been cofunded by the European Union (ERC, Electrophot, Grant No. 101097569). Views and opinions expressed are however those of the author(s) only and do not necessarily reflect those of the European Union or the European Research Council. Neither the European Union nor the granting authority can be held responsible for them. We acknowledge the National Centre for HPC, Big Data and Quantum Computing, under the National Recovery and Resilience Plan (NRRP), Mission 4 Component 2 Investment 1.4 CUP I53C22000690001 funded from the European Union, NextGenerationEU.

DATA AVAILABILITY

The data that support the findings of this article are openly available [39].

[1] H. D. Yallew, M. Vlk, A. Datta, S. Alberti, R. A. Zakoldaev, J. Høvik, A. Aksnes, and J. Jágerská, Sub-PPM methane detection with mid-infrared slot waveguides, ACS Photonics **10**, 4282 (2023).

[2] F. Ottonello-Briano, C. Errando-Herranz, H. Rödjegård, H. Martin, H. Sohlström, and K. B. Gylfason, Carbon dioxide absorption spectroscopy with a mid-infrared silicon photonic waveguide, Opt. Lett. **45**, 109 (2020).

[3] Y.-C. Chang, P. Wägli, V. Paeder, A. Homsy, L. Hvozdara, P. van der Wal, J. Di Francesco, N. F. de Rooij, and H. P. Herzig, Cocaine detection by a mid-infrared waveguide integrated with a microfluidic chip, Lab Chip **12**, 3020 (2012).

[4] L. Labadie, G. Martín, A. Ródenas, N. C. Anheier, Jr., B. Arezki, R. R. Thomson, H. A. Qiao, P. Kern, A. K. Kar, and B. E. Bernacki, Advances in the development of mid-infrared integrated devices for interferometric arrays, Proc. SPIE Int. Soc. Opt. Eng. **8445**, 844515 (2012).

[5] S. Jung, D. Palaferri, K. Zhang, F. Xie, Y. Okuno, C. Pinzone, K. Lascola, and M. A. Belkin, Homogeneous photonic integration of mid-infrared quantum cascade lasers with low-loss passive waveguides on an InP platform, Optica **6**, 1023 (2019).

[6] A. Gutierrez-Arroyo, E. Baudet, L. Bodiou, I. Hardy, J. Lemaitre, F. Faijan, B. Bureau, V. Nazabal, and J. Charrier, Optical characterization at 7.7 μm of an integrated platform based on chalcogenide waveguides for sensing applications in the mid-infrared, Opt. Express **24**, 23109 (2016).

[7] T. Hu, B. Dong, X. Luo, T.-Y. Liow, J. Song, C. Lee, and G.-Q. Lo, Silicon photonic platforms for mid-infrared applications, Photonics Res. **5**, 417 (2017).

[8] R. Soref, Mid-infrared photonics in silicon and germanium, Nat. Photonics **4**, 495 (2010).

[9] D. Marris-Morini, V. Vakarin, J. M. Ramirez, Q. Liu, A. Ballabio, J. Frigerio, M. Montesinos, C. Alonso-Ramos, X. Le Roux, S. Serna, D. Benedikovic, D. Chrastina, L. Vivien, and G. Isella, Germanium-based integrated photonics from near- to mid-infrared applications, Nanophotonics **7**, 1781 (2018).

[10] T. H. N. Nguyen, V. Turpaud, N. Koompai, J. Peltier, S. Calcaterra, G. Isella, J.-R. Coudevylle, C. Alonso-Ramos, L. Vivien, J. Frigerio, and D. Marris-Morini, Integrated PIN modulator and photodetector operating in the mid-infrared range from 5.5 μm to 10 μm, Nanophotonics **13**, 1803 (2024).

[11] L. Reid, M. Nedeljković, W. Cao, L. Mastronardi, R. Slavík, and G. Mashanovich, Photodetection at 3.8 μm using intrinsic monolithic integrated germanium photodiodes, in *IEEE 17th International Conference on Group IV Photonics, Malaga, Spain (GFP 2021)* (IEEE, Piscataway, NJ, 2021).

[12] G. Ciasca, M. De Seta, G. Capellini, F. Evangelisti, M. Ortolani, M. Virgilio, G. Grosso, A. Nucara, and P. Calvani, Terahertz intersubband absorption and conduction band alignment in *n*-type Si/SiGe multiple quantum wells, Phys. Rev. B **79**, 085302 (2009).

[13] Y. Busby, M. De Seta, G. Capellini, F. Evangelisti, M. Ortolani, M. Virgilio, G. Grosso, G. Pizzi, P. Calvani, S. Lupi, M. Nardone, G. Nicotra, and C. Spinella, Near- and far-infrared absorption and electronic structure of Ge-SiGe multiple quantum wells, Phys. Rev. B **82**, 205317 (2010).

[14] M. De Seta, G. Capellini, M. Ortolani, M. Virgilio, G. Grosso, G. Nicotra, and P. Zaumseil, Narrow intersubband transitions in n-type Ge/SiGe multi-quantum wells: Control of the terahertz absorption energy trough the temperature dependent depolarization shift, Nanotechnology **23**, 465708 (2012).

[15] S. K. Chun, D. S. Pan, and K. L. Wang, Intersubband transitions in a *p*-type δ-doped SiGe/Si quantum well, Phys. Rev. B **47**, 15638 (1993).

[16] M. Helm, P. Kruck, T. Fromherz, A. Weichselbaum, M. Seto, G. Bauer, Z. Moussa, P. Boucaud, F. H. Julien, J.-M. Lourtioz, J. F. Nützel, and G. Abstreiter, IR studies of p-type Si/SiGe quantum wells: intersubband absorption, IR detectors, and second-harmonic generation, Thin Solid Films **294**, 330 (1997).

[17] T. Fromherz, M. Meduňa, G. Bauer, A. Borak, C. V. Falub, S. Tsujino, H. Sigg, and D. Grützmacher, Intersubband absorption of strain-compensated $Si_{1-x}Ge_x$ valence-band quantum wells with $0.7 \leqslant x \leqslant 0.85$, J. Appl. Phys. **98**, 044501 (2005).

[18] P. Boucaud, L. Wu, F. H. Julien, J.-M. Lourtioz, I. Sagnes, Y. Campidelli, R. Prazeres, and J.-M. Ortega, Spectroscopy of intersubband transitions in Si − $Si_{1-x}Ge_x$ quantum wells, Thin Solid Films **294**, 173 (1997).

[19] K. Gallacher, A. Ballabio, R. W. Millar, J. Frigerio, A. Bashir, I. MacLaren, G. Isella, M. Ortolani, and D. J. Paul, Mid-infrared intersubband absorption from p-Ge quantum wells grown on Si substrates, Appl. Phys. Lett. **108**, 091114 (2016).

[20] J. Frigerio, C. Ciano, J. Kuttruff, A. Mancini, A. Ballabio, D. Chrastina, V. Falcone, M. De Seta, L. Baldassarre, J. Allerbeck, D. Brida, L. Zeng, E. Olsson, M. Virgilio, and M. Ortolani, Second Harmonic generation in germanium quantum Wells for nonlinear silicon photonics, ACS Photonics **8**, 3573 (2021).

[21] A. Barzaghi, V. Falcone, S. Calcaterra, D. Marris-Morini, M. Virgilio, and J. Frigerio, Modelling of an intersubband quantum confined Stark effect in Ge quantum wells for mid-infrared photonics, Opt. Express **30**, 46710 (2022).

[22] M. Virgilio and G. Grosso, Valence and conduction intersubband transitions in SiGe, Ge-rich, quantum wells on [001]

$Si_{0.5}Ge_{0.5}$ substrates: A tight-binding approach, J. Appl. Phys. **100**, 093506 (2006).

[23] M. Virgilio and G. Grosso, Valley splitting and optical intersubband transitions at parallel and normal incidence in [001]-Ge/SiGe quantum wells, Phys. Rev. B **79**, 165310 (2009).

[24] G. Pizzi, M. Virgilio, and G. Grosso, Tight-binding calculation of optical gain in tensile strained [001]-Ge/SiGe quantum wells, Nanotechnology **21**, 055202 (2010).

[25] T. B. Boykin, G. Klimeck, and F. Oyafuso, Valence band effective-mass expressions in the $sp^3d^5s^*$ empirical tight-binding model applied to a Si and Ge parametrization, Phys. Rev. B **69**, 115201 (2004).

[26] J.-M. Jancu, R. Scholz, F. Beltram, and F. Bassani, Empirical $spds^*$ tight-binding calculation for cubic semiconductors: General method and material parameters, Phys. Rev. B **57**, 6493 (1998).

[27] G. Isella, D. Chrastina, B. Rössner, T. Hackbarth, H. J. Herzog, U. König, and H. von Känel, Low-energy plasma-enhanced chemical vapor deposition for strained Si and Ge heterostructures and devices, Solid State Electron. **48**, 1317 (2004).

[28] F. Isa, J. A. Schmidt, S. Aghion, E. Napolitani, G. Isella, and R. Ferragut, Hole and positron interaction with vacancies and p-type dopants in epitaxially grown silicon, J. Appl. Phys. **135**, 165704 (2024).

[29] C. G. Darwin, XXXIV. The theory of X-ray reflexion, Philos. Mag. **27**, 315 (1914).

[30] D. Kriegner, E. Wintersberger, and J. Stangl, xrayutilities: A versatile tool for reciprocal space conversion of scattering data recorded with linear and area detectors, J. Appl. Crystallogr. **46**, 1162 (2013).

[31] C. Ndebeka-Bandou, F. Carosella, R. Ferreira, A. Wacker, and G. Bastard, Free carrier absorption and inter-subband transitions in imperfect heterostructures, Semicond. Sci. Technol. **29**, 023001 (2014).

[32] E. R. Weber, R. K. Willardson, H. C. Liu, and F. Capasso, *Intersubband Transitions in Quantum Wells* (Academic Press, Cambridge, UK, 1999).

[33] M. Geiser, C. Walther, G. Scalari, M. Beck, M. Fischer, L. Nevou, and J. Faist, Strong light-matter coupling at terahertz frequencies at room temperature in electronic LC resonators, Appl. Phys. Lett. **97**, 191107 (2010).

[34] N. A. Polonsky, S. A. Virko, O. N. Poklonskaya, and A. G. Zabrodskii, Transition temperature from band to hopping direct current conduction in crystalline semiconductors with hydrogen-like impurities: Heat versus Coulomb attraction, J. Appl. Phys. **110**, 123702 (2011).

[35] A. V. Buyanov, A. C. Ferreira, E. Söderström, I. A. Buyanova, P. O. Holtz, B. Sernelius, B. Monemar, M. Sundaram, K. Campman, J. L. Merz, and A. C. Gossard, Thermally activated intersubband and hopping transport in center-doped *p*-type $GaAs/Al_xGa_{1-x}As$ quantum wells, Phys. Rev. B **53**, 1357 (1996).

[36] T. F. Lee and T. C. McGill, Variation of impurity—to—band activation energies with impurity density, J. Appl. Phys. **46**, 373 (1975).

[37] S. J. Allen Jr., D. C. Tsui, and B. Vinter, On the absorption of infrared radiation by electrons in semiconductor inversion layers, Solid State Commun. **20**, 425 (1976).

[38] T. Fromherz, E. Koppensteiner, M. Helm, G. Bauer, J. F. Nützel, and G. Abstreiter, Hole energy levels and intersubband absorption in modulation-doped $Si/Si_{1-x}Ge_x$ multiple quantum wells, Phys. Rev. B **50**, 15073 (1994).

[39] S. Calcaterra and M. Faverzani, Data underlying the paper titled "Optical and structural properties of p-doped Ge/SiGe multiple quantum wells for mid-infrared photonics" [Data set], Zenodo (2025), https://doi.org/10.5281/zenodo.14864906.